Supplementary Information

Polarization-selective, tailorable, and flexible InP nanofilm UV photodetectors

Tuomas Haggren [a], Wei Wen Wong [a], Yang Yu [a], Veda C Dinesh [ab], Siti Samsuri [c], Chenglong Xu [d], Madhu Bhaskaran [d], Chennupati Jagadish [a], Lan Fu [a], Hark Hoe Tan [a]**

a. ARC Centre of Excellence for Transformative Meta-Optical Systems, Department of Electronic Materials Engineering, Research School of Physics, The Australian National University, Canberra, ACT 2600, Australia
b. International School of Photonics, Cochin University of Science and Technology, Cochin 682 022, Kerala, India
c. School of Physics, Universiti Sains Malaysia (USM), Pulau Pinang, 11800, Malaysia
d. ARC Centre of Excellence for Transformative Meta-Optical Systems, Functional Materials and Microsystems Research Group, RMIT University, Melbourne, VIC 3001, Australia
*Corresponding author

KEYWORDS nanomembranes; ultrathin semiconductors; wearables; quantum confinement; non-layered 2D materials

Transmittance

Transmittance at selected wavelengths (300 nm, 400 nm and 600 nm) are shown in Figure S1. The 550 nm thick film has minimal transmittance at each wavelength. The nanofilms (5 – 50 nm thick) transmit significant part of the visible 600 nm illumination (20 – 60%), whereas the shorter wavelengths are absorbed efficiently.

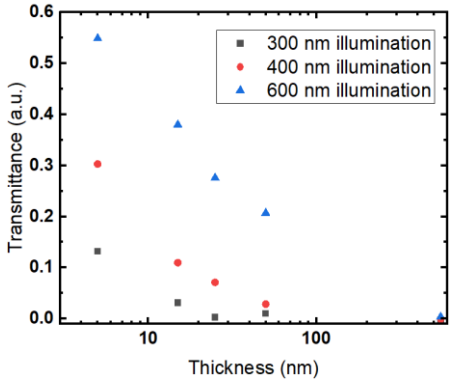

Figure S1: Transmittance at selected wavelengths through the 5 – 550 nm thick InP nanofilms.

Photoluminescence

Photoluminescence signal from a reference sample with BCB polymer but no InP nanofilm is shown in Figure S2. The observed signal is due to the BCB polymer, and therefore, the signal observed at these wavelengths from InP nanofilms is attributed to BCB and not InP. Note that the thinnest InP nanofilms are semi-transparent in the visible wavelength range, allowing both the excitation to reach the BCB polymer and the resulting fluorescence to be measured.

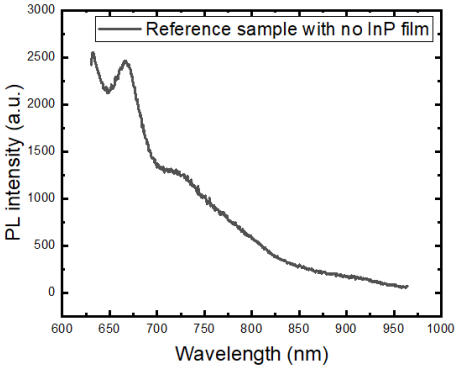

Figure S2: Photoluminescence spectrum from a reference sample with BCB polymer and without InP nanofilm.

Raman peak shift

Figure S3 shows Raman LO peak positions for the 5 – 550 nm thick InP nanofilms. The minor shift in the peak is attributed to size effects.

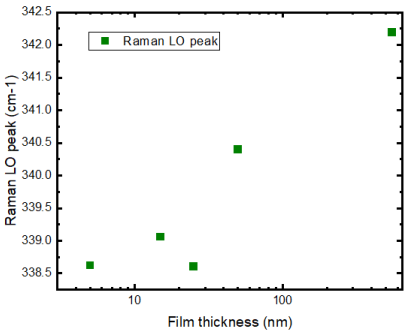

Figure S3: Raman LO peak positions measured from InP nanofilms with 5 – 550 nm thickness range.

Time-resolved photoluminescence

Figure S4 shows carrier lifetimes obtained from time-resolved photoluminescence (TRPL) by single-exponential fitting. The carrier lifetimes are reduced substantially from >1 ns to ~60 ps suggesting the capability to create high-speed photodetectors. It should be noted here that the apparent saturation of the lifetime to 60 ps may be due to system limitations.

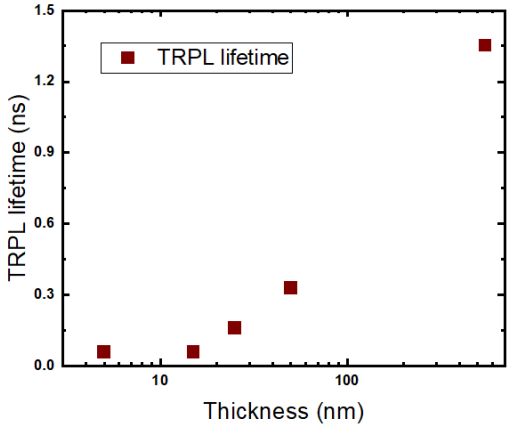

Figure S4: Carrier lifetimes obtained from time-resolved photoluminescence measurements for 5 – 550 nm thick InP nanofilms.

Fermi level pinning, band bending and effective carrier concentration modelling

A one-dimensional, self-consistent Poisson solver was implemented to model the electrostatic band profile and electron distribution in ultrathin InP nanofilms. The model assumes a uniformly n-doped InP layer with classical (non-degenerate) electron statistics and a three-dimensional density of states. Surface Fermi-level pinning is imposed at both film interfaces by fixing the conduction-band–to–Fermi-level separation, $E_C - E_F$, to a prescribed value.

The Poisson equation is solved using a finite-difference scheme with Dirichlet boundary conditions at the film surfaces. At each iteration, the local electron density is calculated from the conduction band profile assuming Boltzmann statistics, and the electrostatic potential is updated self-consistently until convergence. The model outputs the spatial profiles of $E_C(z) - E_{FE}$ and $n(z)$, as well as the volume-averaged effective electron concentration. This approach captures surface-pinning–dominated band bending across the full film thickness and is used to assess carrier distributions in the ultrathin films.

The solver is attached as an appendix at the end of the Supplementary Information file.

Figure S5 shows the modelled band profiles of the InP films at 5 – 550 nm thicknesses. Due to the low doping level, the band bending is minimal (<0.1 meV) in the 5 – 50 nm thick films. The effective carrier concentrations, resistivities and mobilities of the films are presented in table S1.

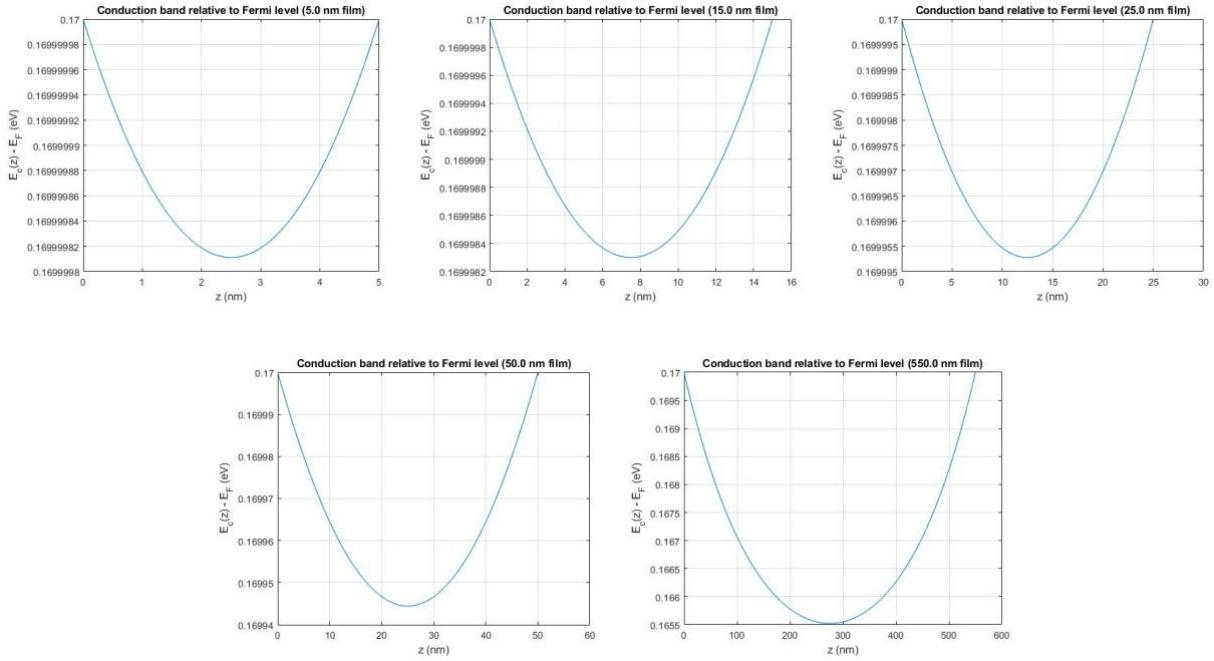

Figure S5: Band bending profiles in 5 – 550 nm thick InP nanofilms.

Table S1. Effective electron concentrations, resistivities and mobilities of InP nanofilms.

Thickness	n_eff (cm^{-3})	ρ (Ω·m)	μ_eff ($cm^2/V·s$)
550 nm	8.9×10^{14}	0.0152	~4.6×10^{3}
50 nm	7.9×10^{14}	5.51	~14
25 nm	7.9×10^{14}	5.12	~15
15 nm	7.9×10^{14}	36.8	~2.1
5 nm	7.9×10^{14}	1.34×10^{4}	~6×10^{-3}

Current-voltage characterization

Figure S6 shows current-voltage measurements from InP nanofilms with thicknesses of 5, 15, 25, 50 and 550 nm. Both dark current and current under 405 nm illumination are shown. Figure S7 shows current-voltage measurement from the 15 nm nanofilm additionally after >12-month delay.

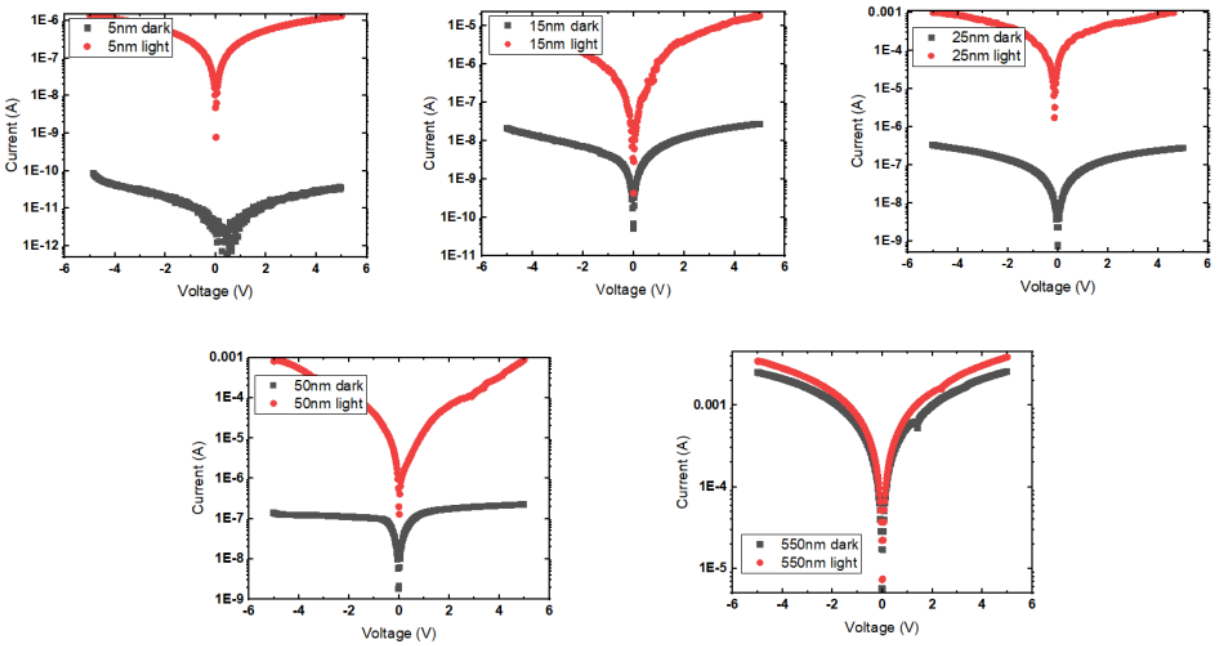

Figure S6: IV curves from 5 – 550 nm thick InP nanofilms in dark and under 405 nm illumination.

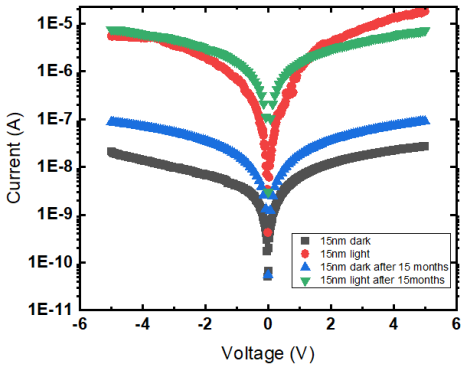

Figure S7: IV curves measured from 15 nm thick InP nanofilms in dark and under 405 nm illumination shortly after the fabrication and after >12-month delay.

Responsivity

Figure S8 left side shows wavelength-dependent responsivity curves for 5 – 550 nm thick InP nanofilms. To ensure similar reflection from the backside of the nanofilms, an Al mirror was placed after a SiO_2 spacer. The used layer stack was air / 5 – 550 nm InP nanofilm / 190 nm SiO_2 / Al 50 nm. This resulted in additional Fabry-Perot absorption peaks in the visible range that are seen as responsivity peaks and valleys. These resonances are also observed in reflectance measurements shown in Figure S4 on the right side. For the UV-to-visible responsivity ratio, wavelength regions without strong resonances were chosen (~375 nm and 730 nm). On the other hand, the significantly increased responsivities corresponding to reflectance minima (i.e. absorptance maxima) demonstrate the possibility of using resonant structures for wavelength-selective absorption. This can be utilized in realizing InP nanofilm microspectrometers.

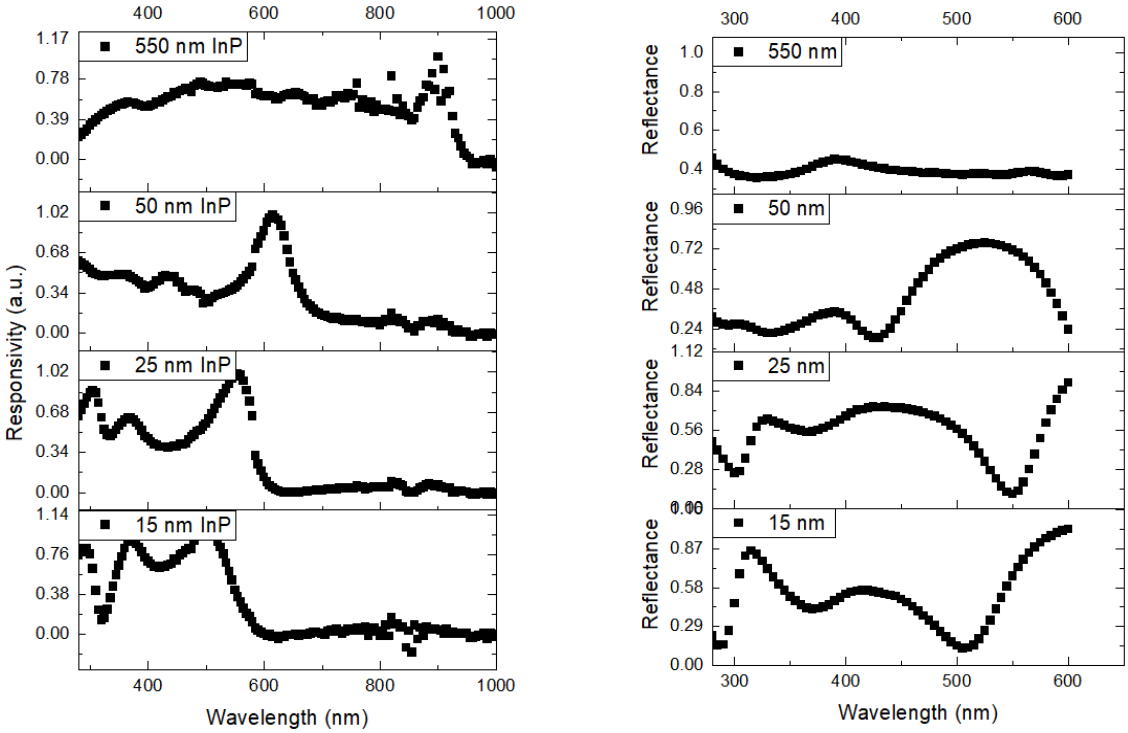

Figure S8: Responsivity curves from 15 – 550 nm thick InP nanofilms with SiO_2 spacers and Al back reflectors (left) and reflectance spectra from the same samples.

Table S2 presents comparison of responsivity, external quantum efficiency (EQE), transmittance and gain comparison at 365 nm illumination. Gain is given with the assumptions of zero reflectance, and by assuming reflectance of 45 %.

Table S2. R, EQE, transmittance and gain of InP nanofilms at 365 nm wavelength.

Thickness (nm)	Responsivity R (A/W)	EQE (%)	Transmittance T	Gain (Ropt = 0)	Gain (Ropt = 0.45)
5	9.58107E-06	0.00325	0.42280	5.63E-05	2.56E-04
15	7.01700E-02	23.8	0.17311	0.288	0.633
25	5.85284E+00	1 990	0.08527	21.7	42.8
50	6.57863E+00	2 230	0.02177	22.8	42.3
550	6.07861E+01	20 700	0.00000	207	376

Polarization-selective detectors

Figure S9 illustrates a scalable fabrication and integration concept for edge-illuminated, polarization-selective InP nanofilm detectors. The devices are first fabricated on carrier wafers (e.g., Si, glass, or flexible substrates) using standard thin-film processing, with an opaque layer beneath the nanofilm to suppress bottom-side illumination. After device definition, the nanofilms are capped with an opaque top layer, ensuring that optical excitation occurs exclusively through the film edge.

The carrier wafer is then diced into individual detector chips using standard wafer-singulation techniques. Although Figure S9 depicts a nanofilm region being divided into multiple chips, in practice a single wafer can host hundreds to thousands of such devices, making the approach compatible with high-throughput manufacturing.

For polarization-selective operation, the chips are mounted in a side-illuminated geometry during final system integration, for example by placing them vertically on a printed circuit board (PCB) or carrier substrate. In this orientation, light is coupled directly into the cleaved nanofilm edge, while the opaque encapsulation suppresses polarization-insensitive excitation from other directions. The effective polarization selectivity is therefore governed by the nanofilm orientation relative to the incident field, rather than by additional optical components.

From a system perspective, this geometry is compatible with compact integration using simple lenses or waveguides for edge coupling, and can be extended to detector arrays by arranging multiple chips with a common optical access direction. While detailed optimization of optical coupling efficiency and absolute responsivity is beyond the scope of this work, the concept provides a clear pathway toward practical, polarization-selective nanofilm photodetectors without external polarizers.

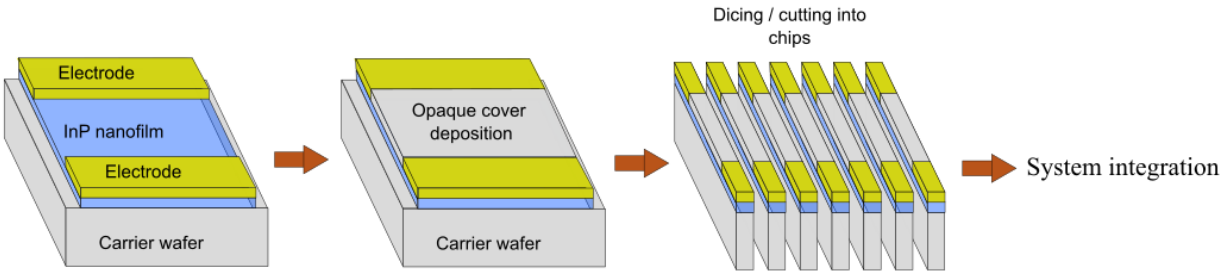

Figure S9: Schematic of a fabrication process flow for practical polarization-selective devices. Note that while the schematic shows only one InP nanofilm area that is cut into several chips, in reality the carrier wafer can host hundreds to thousands of final chips.

Figure S10 shows experimental wavelength-dependent dichroic responsivity ratio for a 25 nm thick InP nanofilm with edge-on illumination, as well as simulated absorption for a similar structure. Note that the experimental data is noisy due to the weak response (i.e. small value) in perpendicular polarization, which is the divider in the plot. Polarization-dependent absorption spectra of the InP nanofilms were simulated with the Finite Difference Time Domain (FDTD) method using the commercial ANSYS Lumerical software package. The refractive index of InP was adopted from the literature [1]. InP nanofilms were oriented in the *xy*-plane, and perfectly matched layers (PML) were applied as the *x*, *y*, and *z* boundary conditions, with three sides of the nanofilms extending into the PML layers to emulate infinitely large nanofilm area. One side of nanofilm, along with the substrate, was exposed to an air interface where the structure was illuminated with a plane wave source. Absorption of the p- and s-polarized light was simulated by setting the electric field polarization of the plane wave source accordingly.

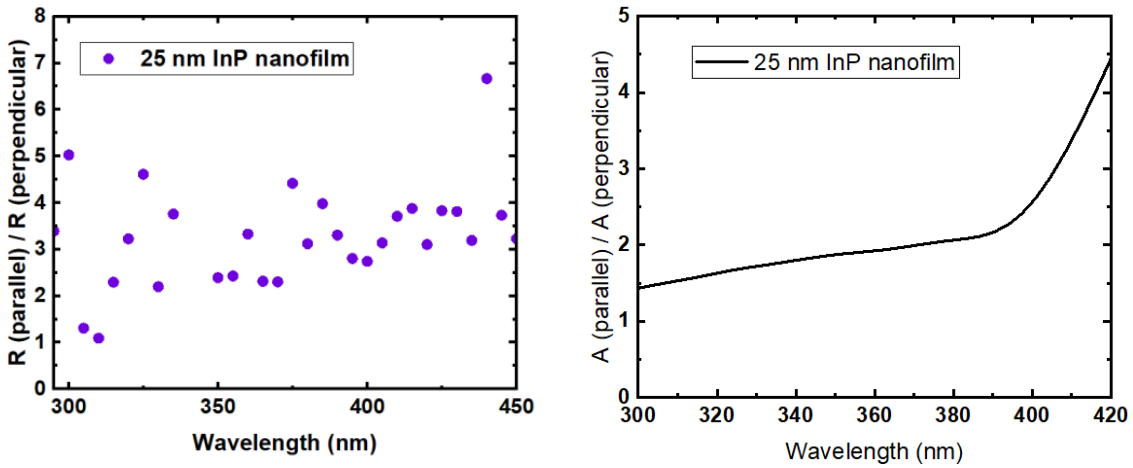

Figure S10: Experimental responsivity ratio (left) and simulated absorbed power ratio (right) between parallel and perpendicular polarizations with illumination towards nanofilm edge.

References

[1] J. Appl. Phys. 66, 6030–6040 (1989)

Appendix: Matlab script for solving Poisson equation

```
%% Classical 1D Poisson solver for InP nanofilm with surface pinning
% - Uniform n-type doping ND
% - Classical 3D DOS (Nc) for electrons
% - Surface pinning: Ec - EF = Delta_surf at both surfaces
% - Outputs Ec(z)-EF, n(z), effective 3D density

clear; clc;

%% ---------- Physical constants ----------
q    = 1.602176634e-19;     % Elementary charge [C]
h    = 6.62607015e-34;      % Planck constant [J*s]
hbar = h / (2*pi);
kB   = 1.380649e-23;        % Boltzmann constant [J/K]
m0   = 9.10938356e-31;      % Electron rest mass [kg]
eps0 = 8.8541878128e-12;    % Vacuum permittivity [F/m]

%% ---------- Material parameters (InP) ----------
T      = 300;               % Temperature [K]
me_eff = 0.08 * m0;         % Electron effective mass [kg]
eps_r  = 12.5;              % Relative permittivity of InP
eps    = eps0 * eps_r;      % Absolute permittivity [F/m]

% Effective density of states Nc (3D)
Nc_SI  = 2 * (2*pi*me_eff*kB*T / h^2)^(3/2);  % [m^-3]
Nc_cm3 = Nc_SI / 1e6;                          % [cm^-3]
fprintf('Nc ? %.3e cm^-3 at T = %g K\n', Nc_cm3, T);

%% ---------- Film geometry ----------
t_nm = 550;                   % Film thickness [nm] -> change for 5, 25,
50, 550, ...
t    = t_nm * 1e-9;         % [m]

N    = 501;                 % Number of grid points
z    = linspace(0, t, N)';  % [m]
dz   = z(2) - z(1);         % [m]

%% ---------- Doping and Fermi level ----------
ND_cm3 = 1e15;              % Donor concentration [cm^-3]
ND     = ND_cm3 * 1e6;      % [m^-3]

% Fermi level relative to a flat-band Ec0 (Ec0 = 0 eV)
EF_eV  = -0.16;             % Chosen to give ~1e15 cm^-3 in bulk
EF_J   = EF_eV * q;         % [J]

%% ---------- Surface pinning: Ec - EF = Delta_surf at surfaces ----------
Delta_surf_eV = 0.17;       % Ec - EF at surfaces [eV] (Chosen to give
~1e15 cm^-3 for 550 nm film)
% Convert to boundary potential phi_surf:
% Ec = Ec0 - q*phi, Ec0 = 0 -> Ec - EF = -q*phi - EF_J = Delta_surf*q
% => phi_surf = -(EF_eV + Delta_surf_eV) [V]
```

```
phi_left  = -(EF_eV + Delta_surf_eV);
phi_right = -(EF_eV + Delta_surf_eV);
fprintf('Surface pinning: Ec - EF = %.2f eV at both interfaces.\n',
Delta_surf_eV);

%% ---------- Finite-difference Laplacian (scaled) ----------
evec = ones(N,1);
D2   = spdiags([evec -2*evec evec], -1:1, N, N);   % dimensionless

%% ---------- Self-consistent Poisson loop (classical) ----------
maxIter   = 200;
tol_phi   = 1e-5;           % Convergence tolerance for potential [V]
alpha_mix = 0.2;            % Mixing factor for stability (0<alpha<=1)

% Initial guess for potential: linear between surface values
phi = linspace(phi_left, phi_right, N)';   % [V]

n_z  = zeros(N,1);          % Electron density [m^-3]

fprintf('\nStarting classical Poisson for %.1f nm film...\n', t_nm);

for iter = 1:maxIter

    % --- Electron density from classical statistics ---
    % Ec(z) = -q*phi(z) (Ec0 = 0), so EF - Ec = EF_J + q*phi
    eta_z = (EF_J + q*phi) / (kB * T);         % dimensionless
    n_z   = Nc_SI .* exp(eta_z);               % [m^-3]

    % --- Charge density and Poisson RHS ---
    rho = q * (ND - n_z);                     % [C/m^3]

    A = D2;
    b = -(rho / eps) * dz^2;

    % Dirichlet BCs
    A(1,:) = 0; A(1,1) = 1; b(1) = phi_left;
    A(N,:) = 0; A(N,N) = 1; b(N) = phi_right;

    phi_new = A \ b;

    % Mix for stability
    phi_mixed = alpha_mix * phi_new + (1 - alpha_mix) * phi;

    dphi = max(abs(phi_mixed - phi));
    phi  = phi_mixed;

    fprintf('Iter %3d: max|dphi| = %.3e V\n', iter, dphi);
    if dphi < tol_phi
        fprintf('Converged after %d iterations (max|dphi| = %.3e V).\n',
iter, dphi);
        break;
```

```
    end
end

%% ---------- Post-processing ----------
% Conduction band profile and Ec - EF
Ec_J   = -q * phi;              % Ec(z) [J], with Ec0=0
Ec_eV  = Ec_J / q;              % [eV]
Ec_minus_EF_eV = Ec_eV - EF_eV; % Ec - EF in eV

% Effective 3D density (volume average)
n_eff = trapz(z, n_z) / t;      % [m^-3]
n_eff_cm3 = n_eff / 1e6;        % [cm^-3]

% Mid-film density as "bulk-like" reference
n_mid_cm3 = n_z(round(N/2)) / 1e6;   % [cm^-3]

fprintf('\nResults for %.1f nm InP nanofilm (classical, pinned
surfaces):\n', t_nm);
fprintf('Volume-averaged n_eff   = %.3e cm^-3\n', n_eff_cm3);
fprintf('Mid-film n(z=L/2)       = %.3e cm^-3\n', n_mid_cm3);

% Rough resistivity estimate using a guessed mobility
mu_cm2_Vs = 3000;                    % adjust based on film quality
mu_SI     = mu_cm2_Vs * 1e-4;        % [m^2/Vs]
rho_SI    = 1 / (q * n_eff * mu_SI); % [Ohm*m]
fprintf('If mu = %.0f cm^2/Vs, rho ? %.3e Ohm*m\n', mu_cm2_Vs, rho_SI);

%% ---------- Plots ----------
% 1) Ec - EF profile
figure;
plot(z*1e9, Ec_minus_EF_eV);
xlabel('z (nm)');
ylabel('E_c(z) - E_F (eV)');
title(sprintf('Conduction band relative to Fermi level (%.1f nm film)',
t_nm));
grid on;

% 2) Electron density profile n(z)
figure;
plot(z*1e9, n_z/1e6);
xlabel('z (nm)');
ylabel('n(z) (cm^{-3})');
title(sprintf('Electron density profile n(z) (%.1f nm film)', t_nm));
grid on;
```